ACS NANO

www.acsnano.org

ARTICLE

Anisotropic van der Waals Tellurene-Based Multifunctional, Polarization-Sensitive, In-Line Optical Device

Jing Yu,[⊥] Haoran Mu,[*,⊥] Pu Wang,[⊥] Haozhe Li, Zixin Yang, Jing Ren, Yang Li, Luyao Mei, Jingni Zhang, Wenzhi Yu, Nan Cui, Jian Yuan, Jian Wu, Sheng Lan,[*] Guangyu Zhang, and Shenghuang Lin[*]

Cite This: https://doi.org/10.1021/acsnano.4c03973 Read Online

ABSTRACT: **Polarization plays a paramount role in scaling the optical network capacity. Anisotropic two-dimensional (2D) materials offer opportunities to exploit optical polarization-sensitive responses in various photonic and optoelectronic applications. However, the exploration of optical anisotropy in fiber in-line devices, critical for ultrafast pulse generation and modulation, remains limited. In this study, we present a fiber-integrated device based on a single-crystalline tellurene nanosheet. Benefiting from the chiral-chain crystal lattice and distinct optical dichroism of tellurene, multifunctional optical devices possessing diverse excellent properties can be achieved. By inserting the in-line device into a 1.5 μm fiber laser cavity, we generated both linearly polarized and dual-wavelength mode-locking pulses with a degree of polarization of 98% and exceptional long-term stability. Through a twisted configuration of two tellurene nanosheets, we realized an all-optical switching operation with a fast response. The multifunctional device also serves as a broadband photodetector. Notably, bipolar polarization encoding communication at 1550 nm can be achieved without any external voltage. The device's multifunctionality and stability in ambient environments established a promising prototype for integrating polarization as an additional physical dimension in fiber optical networks, encompassing diverse applications in light generation, modulation, and detection.**

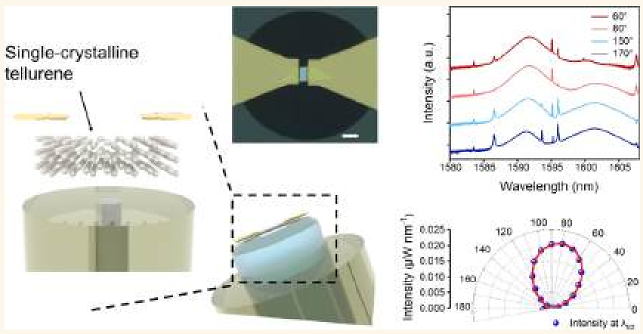

KEYWORDS: *tellurene, polarization-sensitive, mode-locking, photodetector, 2D*

INTRODUCTION

Two-dimensional (2D) materials, owing to their strong light–matter interactions and ease of integration without lattice-matching constraints, offer opportunities for integrated optical and optoelectronic devices.[1−3] Various approaches have led to the integration of a range of 2D materials into optical fibers,[4] including assembling them to fiber cores,[5] fabricating 2D-embedded fibers,[6] and creating evanescently coupled configurations.[7,8] These endeavors have yielded a diverse array of in-line optical fiber devices based on 2D materials, encompassing applications in ultrafast lasers,[5,8] parameter converters,[6] optical modulators,[9,10] and photodetectors.[11] Notably, specific 2D materials, like black phosphorus (BP),[12] β-GaSe,[13] α-In_2Se_3,[14] and ReS_2,[15] exhibit a low in-plane lattice symmetry and manifest optical polarization-sensitive responses. Devices utilizing these anisotropic 2D materials introduce polarization as an additional dimension for modulation and multiplexing within optical networks, thereby complementing the conventional dimensions of intensity and wavelength.[16−18] However, though both the mode-locking and Q-switching pulse have been achieved based on these optically anisotropic materials,[19−22] the exploration of optical anisotropy of 2D materials in devices for ultrafast pulse generation and optical modulation has been limited.[23,24] In a previous study, polarized mode-locking pulses were successfully generated using a BP flake with ~98% degree of polarization, thus harnessing the optical anisotropy of 2D materials for ultrafast laser sources.[25] Nevertheless, further research is needed to integrate polarization sensitivity into multifunctional device performance and

Received: March 25, 2024
Revised: July 3, 2024
Accepted: July 8, 2024

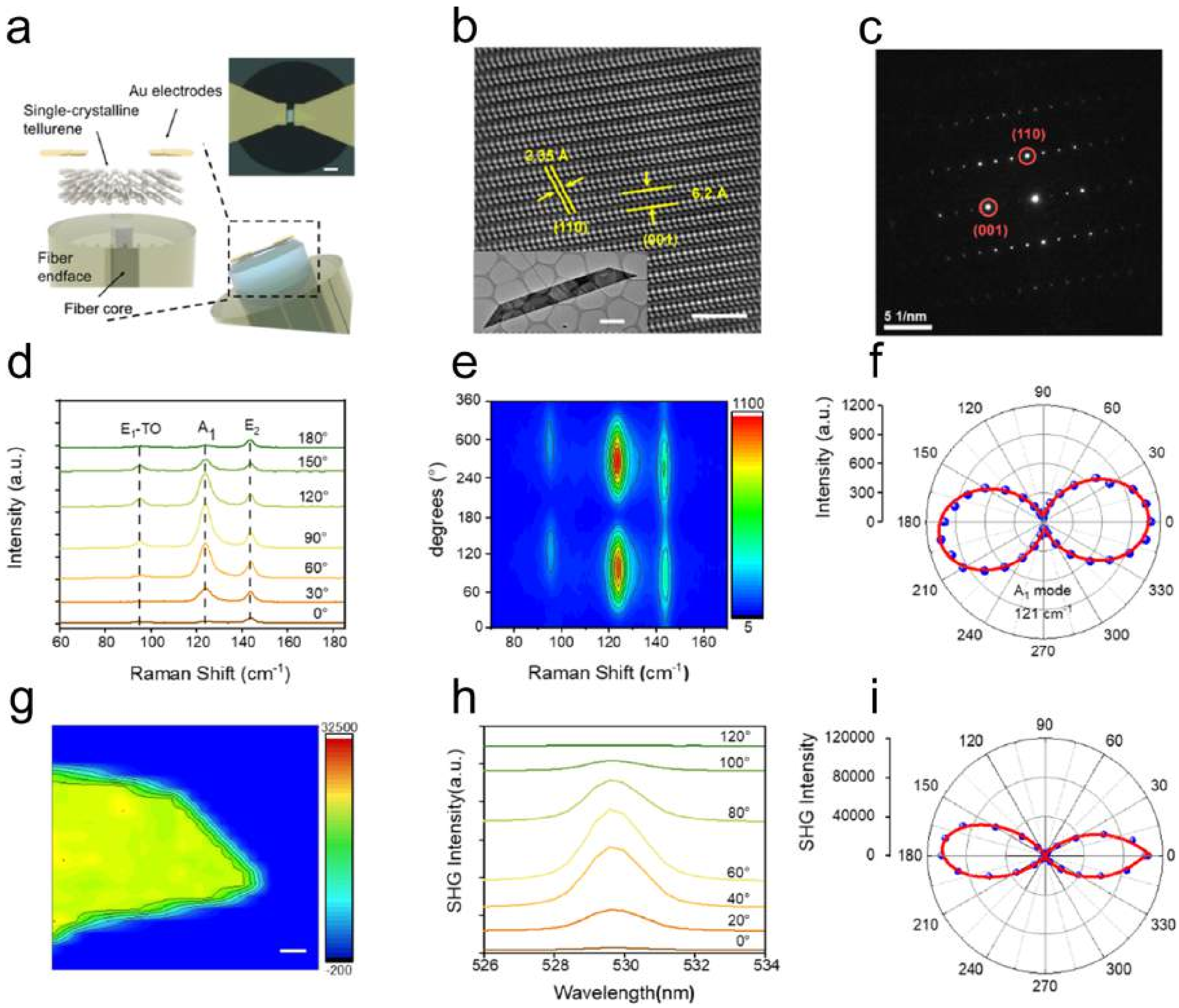

Figure 1. Structure and characterization of the tellurene nanosheet in-line optical device. (a) Conceptual diagram illustrating the tellurene optical device, where a solution-grown tellurene nanosheet is applied to the core of an optical fiber, accompanied by 50 nm thick electrodes on both sides. Inset: optical image of the fabricated device (scale bar: 10 μm). (b) High-resolution TEM image showcasing the atomic structure of tellurene (scale bar: 2 nm) with the inset showing the corresponding bright-field TEM image of the nanosheet (scale bar: 2 μm). (c) Diffraction pattern of tellurene (scale bar: 5 nm^{-1}). (d–f) Angle-resolved Raman measurements presenting Raman spectra with incident angles of a linear-polarized 532 nm laser (d), Raman mapping results indicating intensity variations with the angle of polarization (e), and a polar figure of Raman intensity corresponding to A_1 mode located at 121 cm^{-1} (f). (g–i) Angle-resolved SHG measurements: (g) mapping plots of SHG intensities of 2D Te sheets, (h) angle-resolved SHG spectra, and (i) polar plots of SHG intensities.

to achieve practical polarization-sensitive devices that exhibit high long-term stability in ambient environments.

Tellurene, an emerging 2D monoelemental semiconductor with a narrow band gap and superior air stability, possesses a distinct chiral-chain crystal lattice.[26] Within this lattice, tellurium atoms are helically arranged to form pseudo-1D chains which subsequently couple into 2D-like sheets through vdW bonds.[27,28] This low-symmetry lattice configuration endows tellurene with significant optical dichroism and birefringence.[29] To date, researchers have achieved polarization photodetection with 2D tellurene, enabling broad-spectrum imaging across the visible to mid-infrared range at room temperature.[30,31] Moreover, 2D tellurene and its derivatives exhibit substantial nonlinear optical coefficients, thus holding potential for applications in ultrafast lasers and optical modulators.[32−39] This underscores the significant potential of 2D tellurene-based in-line optical devices for optical anisotropy-driven functionalities.

In this study, we introduce a fiber-integrated tellurene device as a prototype, harnessing the material's optical anisotropy to achieve multiple functions. These functions include the generation of linearly polarized mode-locking pulses, dual-wavelength mode-locking pulses, optical modulation, and broadband polarization photodetection. The device's structure consists of a tellurene nanosheet, gold electrodes, and an optical fiber end-face. We commence our investigation by presenting both the structural and optical anisotropies of tellurene using comprehensive microscopy and spectral techniques. Subsequently, we construct a 1.5 μm mode-locked fiber laser incorporating the fiber-coupled tellurene device,

https://doi.org/10.1021/acsnano.4c03973
ACS Nano XXXX, XXX, XXX−XXX

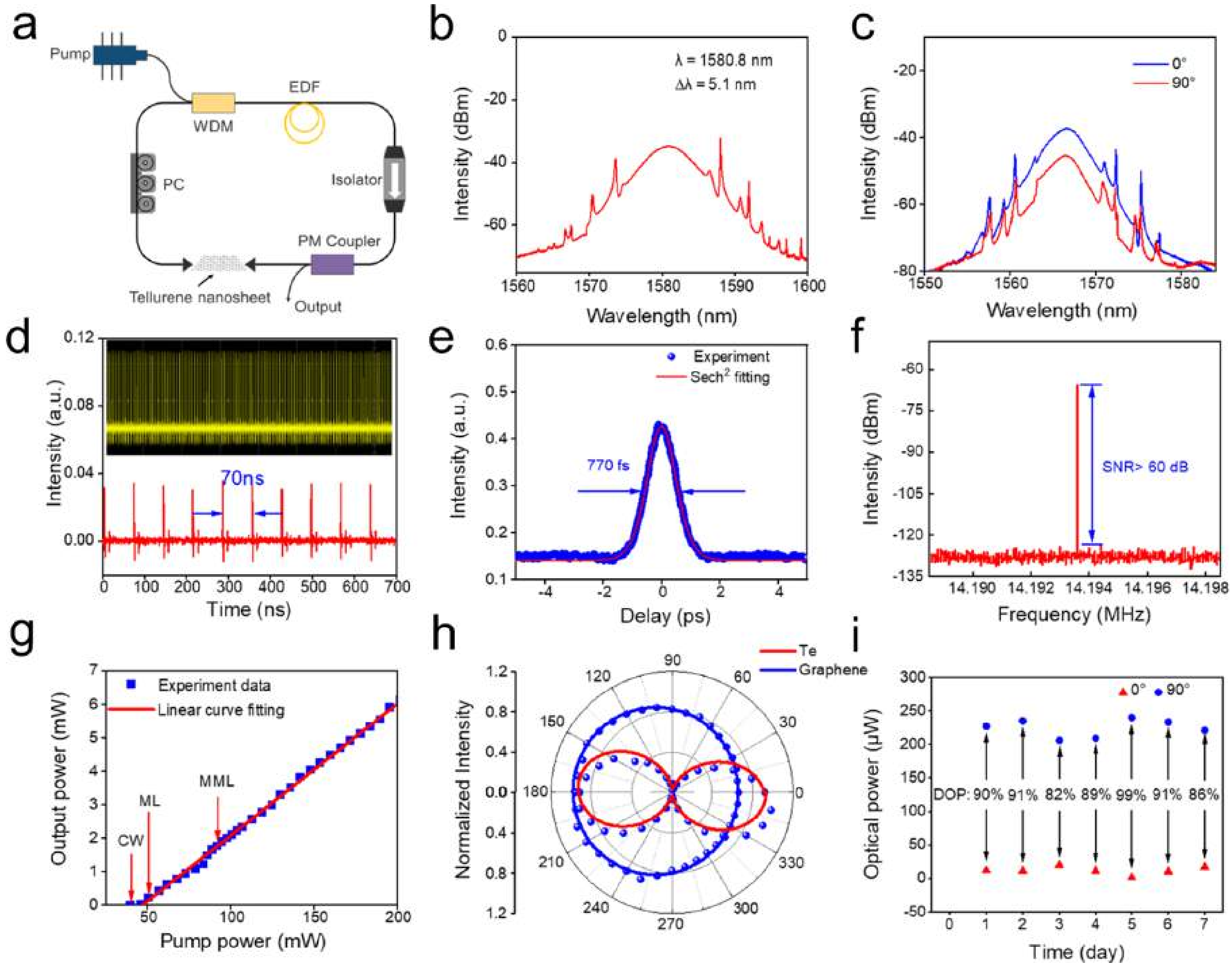

Figure 2. Demonstration of a linear-polarized mode-locked fiber laser based on the tellurene nanosheet device. (a) Experimental setup. (b) Soliton mode-locking optical spectrum. (c) Output spectra after transmitting a rotatable polarizer plate. The rotation angles of the half-waveplate are 0° (blue) and 90° (red), respectively. (d) Pulse train. Inset: snapshot from the oscilloscope tracing. (e) Autocorrelation trace. (f) Radio-frequency (RF) spectrum. (g) Relationship between the output power and the pumping power, showing the continuous-wave (CW), mode-locking (ML), and multiharmonic mode-locking (MML) regions. (h) Polar figures of output power as a function of the angle when the saturable absorber is a tellurene nanosheet (red) and a graphene nanosheet (blue). (i) Measured DOP of the mode-locking pulses over 7 days.

enabling both fundamental and dual-wavelength mode-locking operations with exceptional long-term stability. The degree of polarization (DOP) is high, 98%. Furthermore, the device's inherent optical anisotropy equips it to operate as an optical modulator and a broadband polarization photodetector.

RESULTS/DISCUSSION

Characterization of Structural and Optical Anisotropies. Single-crystalline tellurene nanosheets were successfully synthesized using a solution-growth method.[26] Then, a tellurene nanosheet of appropriate size and thickness was directly transferred onto a flat fiber end-face. The resulting tellurene-based optical structure is schematically illustrated in Figure 1a, showcasing the in-line configuration achieved by allowing the fiber-transmitted light to propagate through the tellurene nanosheet. The optical image in the inset of Figure 1a offers a high-definition view of the fiber end-face, demonstrating successful deposition onto the 9 μm diameter fiber core area.

A comprehensive structural, compositional, and quality analysis of these tellurium crystals was initially conducted by utilizing transmission electron microscopy (TEM) and atomic force microscopy (AFM) techniques. The high-angle annular dark-field scanning TEM (HAADF-STEM) image in the inset of Figure 1b clearly reveals a ladder-shaped tellurene nanosheet measuring approximately ~16 μm in length and ~3 μm in width. Tellurene exhibits a distinctive chiral-chain lattice, where individual helical chains possess a 3-fold screw symmetry along ⟨0001⟩. These chains stack together through van der Waals bonds. The atomic-resolution STEM image in Figure 1b highlights interplanar spacings measuring 2.35 and 6.2 Å, corresponding to tellurene (110) and (001) planes, respectively. Notably, no point defects or dislocations were observed over a large area within the single crystals. Additionally, Figure 1c presents the corresponding selected area electron diffraction (SAED) pattern, further confirming the single-crystalline characteristics. The thickness of the

https://doi.org/10.1021/acsnano.4c03973
ACS Nano XXXX, XXX, XXX−XXX

tellurene nanosheet, as determined from the AFM image, is ~20 nm (Figure S1b).

Raman polarization spectroscopy is an effective technique used to study anisotropic phonon vibrations and crystal orientations. Figure 1d portrays three distinct Raman vibration peaks located at 90, 121, and 141 cm^{-1}. Among them, the most intense Raman peak of tellurene located at ~121 cm^{-1} is related to the A_1 mode, corresponding to the chain expansion mode in which each atom moves in the basal plane. Meanwhile, there exist two degenerate E modes, which separate into predominately bond-bending and bond-stretching types with a larger admixture in tellurene. E_1 mode at ~94 cm^{-1} is caused by *a*- and *b*-axis rotations, and the E_2 mode at 142 cm^{-1} is attributed to the asymmetric stretching mainly along the *c*-axis. It is intriguingly that with the change of the excitation light angle, the magnitudes of these three characteristic peaks vary significantly. The mapping of Raman spectra with changing excitation light angles, depicted in Figure 1e, provides a clear depiction of the evolving trend of the three characteristic peaks in response to alterations in excitation light polarization angles. For a more direct observation of the variation trend in the three Raman characteristic peaks, we plotted their variations against the polarization angle of the excitation light. This representation allowed us to create polarized Raman intensity polar coordinate diagrams corresponding to different vibration modes, as depicted in Figures 1f and S2a,b. The experimental data closely match the fitting curve, illustrating varying degrees of anisotropy, where the three modes display a change cycle of 180°.

Second harmonic generation (SHG) microscopy is a powerful tool for investigating the in-plane optical anisotropy of single-crystalline materials. Figure 1g shows the mapping diagram of the SHG intensity of tellurene nanosheets, and it can be clearly observed that the intensity division of SHG is uniform, which means that the crystalline quality of tellurene is excellent, and the high intensity value of SHG indicates that tellurene has a strong nonlinear effect, which has good potential in nonlinear optical applications. Figure 1h illustrates the SHG intensity of tellurene as a function of the polarization angle of the incident light. As the polarization angle of the incident light varies from 0 to 120°, the SHG peak value exhibits a distinct trend, starting with a small intensity, reaching a peak, and subsequently decreasing. For a more visually intuitive representation of this trend in SHG intensity concerning the polarization angle of the incident light (see Figure 1i). The experimental data closely follow the dichroism fitting curve, emphasizing the evident anisotropy of the material. The Raman spectrum and SHG intensity with incident light angles collectively confirm the asymmetric monoclinic structure of the synthetic tellurene nanosheets.

Linear-Polarized Mode-Locking. Upon inserting the in-line tellurene device into a 1550 nm fiber laser cavity, the linear-polarized mode-locking operation was successfully achieved. The cavity structure is shown in Figure 2a, which is comprehensively discussed in the Methods/Experimental section. Stable mode-locking was obtained by changing the intracavity polarization state once the pump power exceeded the mode-locking power threshold of 50 mW. The optical spectrum at 83 mW pump power, depicted in Figure 2b, exhibited a spectral peak at 1580.8 nm with an impressive 3 dB bandwidth of 5.1 nm. The evident symmetry of the Kerr sidebands indicated the operation of the fiber laser in the soliton mode-locking state. To analyze the linear polarization characteristics of the soliton pulses, a rotatable polarizer plate was introduced at the laser output. Rotating the half-waveplate by 90° resulted in a significant reduction in the output spectrum's intensity, confirming the linear polarization nature of the laser output (Figure 2c).

In Figure 2d, the pulse train captured by an oscilloscope displays a period of 70 ns, corresponding to a repetition rate of 14.2 MHz, signifying the fundamental mode-locking state. The pulse train without pronounced modulation on top indicated high-quality mode-locking output. Figure 2e shows an acquired single-pulse envelope and its fit with the $sech^2$ formula, and the pulse duration was estimated to be 770 fs. The time–bandwidth product was 0.49, which exceeded the value of 0.315 of an ideal $sech^2$ pulse, indicating the slightly larger chirp in the mode-locked laser. The radiofrequency spectrum validated the steady state of the fiber laser with a high signal-to-noise ratio of 61 dB (Figure 2f). The average output power exhibited a linear increase with pump power, as depicted in Figure 2g. When the pump power exceeded 92 mW, the pulse began to split, which led to multiharmonic mode-locking (MML) states.

Then, we characterized the linear polarization power of the achieved mode-locking pulses by systematically rotating a rotatable polarizer plate and recording the optical power with a power meter. The schematic diagram is shown in Figure S4 to illustrate this configuration. When the polarization axis between the half-waveplate and the output light was set horizontally, the highest optical power (P_{max}) reached 106.1 μW. Conversely, when the polarization axis was aligned vertically, the minimum optical power (P_{min}) was at 2.14 μW. The DOP for the linearly polarized output was calculated using the formula DOP = $(P_{max} - P_{min})/(P_{max} + P_{min})$, where P_{max} and P_{min} represent the maximum and minimum measured power, respectively. The DOP for the linearly polarized output was found to be an impressive 98% (Figure 2h). Furthermore, to corroborate the source of the linearly polarized output from our Te fiber laser, we compared it to a graphene saturable absorber, a common mode-locking material that typically does not yield significantly linearly polarized output pulses. This comparison underscores that the linearly polarized output from our tellurene fiber laser is primarily attributed to the anisotropic absorption within the tellurene.

In contrast to previously reported anisotropic 2D black phosphorus (BP), our mode-locked laser based on tellurene demonstrates long-term stability. As illustrated in Figure S2b, we conducted continuous monitoring of the output pulse spectra for over 9 h, revealing that the spectra at different time points remained virtually unchanged. This laser exhibited the capability for repeated self-starting and uninterrupted mode-locking operations for more than 9 h. Following the mode-locking experiment, the tellurene material displayed no signs of degradation, and the laser could self-start even after eight months. The polarization stability is also depicted in Figure 2i, where the value of DOP exhibited minimal variations over a span of 1 week, underscoring the superior polarization stability of the tellurene mode-locked laser.

Dual-Wavelength Mode-Locking. Dual-wavelength lasers have a wide range of applications, including dual-comb ranging, coherent anti-Stokes Raman scattering (CARS), sum frequency generation, and difference frequency generation. The tellurene single nanosheet's optical anisotropy-induced birefringent filtering effect makes it easy to achieve dual-wavelength mode-locking within the same laser cavity. The

https://doi.org/10.1021/acsnano.4c03973
ACS Nano XXXX, XXX, XXX−XXX

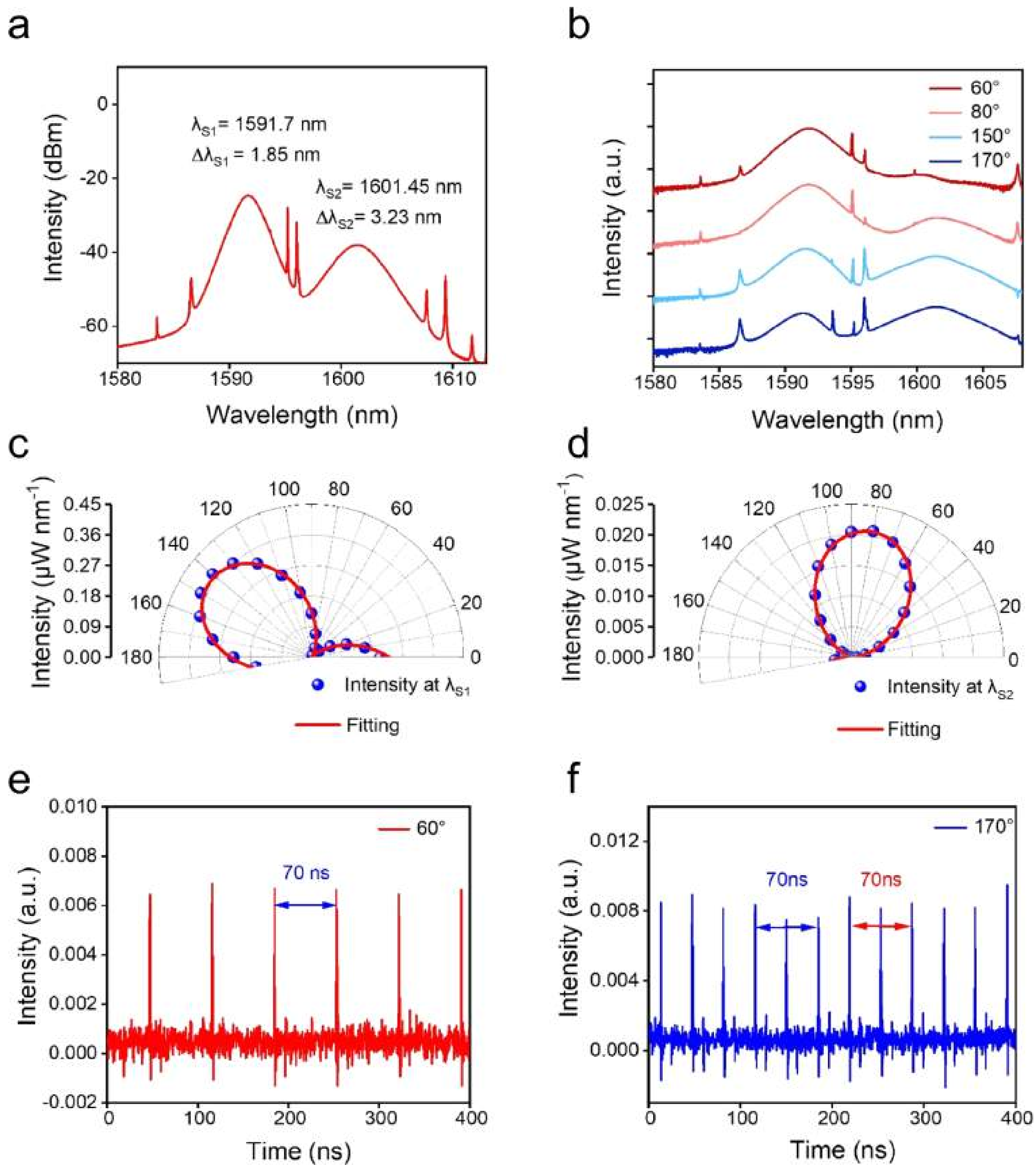

Figure 3. Demonstration of a dual-wavelength mode-locked fiber laser with polarization characteristics. (a) Typical dual-wavelength spectrum, exhibiting peak wavelengths at 1591.7 nm (S1) and 1601.45 nm (S2). (b) Output spectra after transmitting a half-waveplate with different rotation angles. (c) Polar figure of the intensity of the S1 spectrum varying with the angle of the half-waveplate. (d) Polar figure of the intensity of the S2 spectrum varying with the angle of the half-waveplate. (e) Pulse train when the angle of the half-waveplate was 60°. (f) Pulse train when the angle of the half-waveplate was 170°.

power threshold of this mode-locking type is ~70 mW. Once initiated, the dual-wavelength mode-locked operation continues within the cavity until the pump power is reduced to 46 mW, at which point it can be unlocked. Figure 3a illustrates the optical spectrum for the dual-wavelength mode-locking state, where we can observe that the dual-wavelength mode-locked spectrum exhibits peak wavelengths at 1591.7 nm (S1) and 1601.45 nm (S2), with 3 dB spectral bandwidths of 1.85 and 3.23 nm, respectively.

It is interesting that the linearly polarized directions of S1 and S2 pulses are different. We captured the spectra of S1 and S2 under varying polarization directions from 0 to 190°, as presented in Figure 3b. When the polarizer angle was set to 60°, the spectrum shows that the peak of the S1 spectrum reached its maximum height, while the S2 spectrum showed minimal transmission due to the polarizer's orientation being nearly orthogonal to the long axis of its polarization state. Conversely, when the polarizer was set at 170°, the S2 spectrum reached its peak, while the S1 spectral peak weakened significantly because the transmission direction of the half-waveplate differed from the direction of the long axis of the S1 spectral polarization state. The intensity of the spectral peaks of S1 and S2 under different polarization directions is further depicted in Figure 3c,d, confirming their linearly polarized behavior.

https://doi.org/10.1021/acsnano.4c03973
ACS Nano XXXX, XXX, XXX−XXX

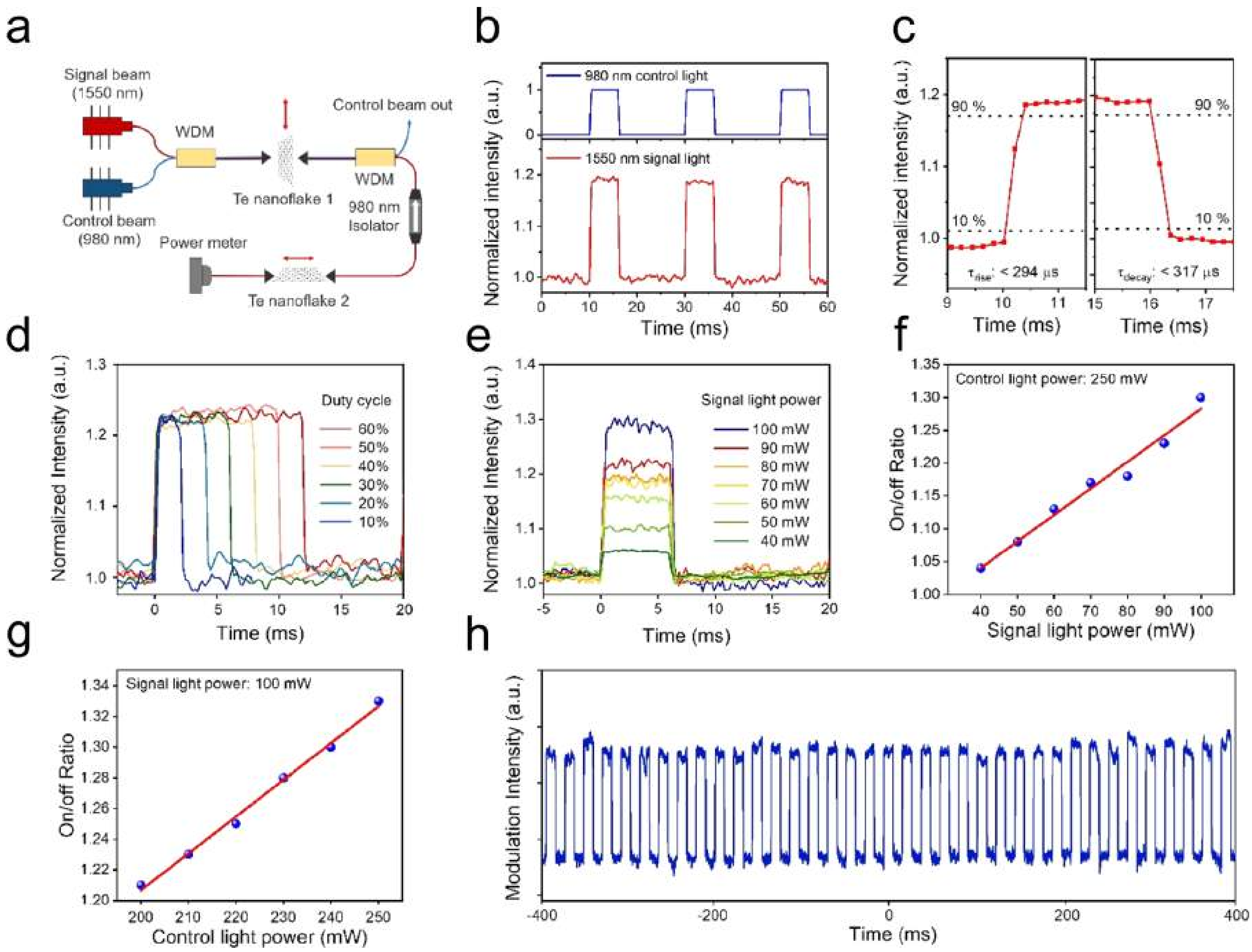

Figure 4. Demonstration of an all-optical switch based on two twisted tellurene nanosheets. (a) Experimental setup. (b) Modulation process of the 1550 nm light by the 980 nm control light. (c) Rise and decay times of the optical switching. (d) Output power of the 1550 nm signal light as a function of the duty cycle of the 980 nm control pulses. (e) Output power of the 1550 nm signal light as a function of the optical power of the 980 nm control pulses. (f) Relationship between the ON/OFF ratio of the 1550 nm signal pulse and the signal light power. (g) Relationship between the ON/OFF ratio of the 1550 nm signal pulse and the 980 nm control light power. (h) Long-term output waveform of the optical switch. The light power and duty cycle of the control pulses were 70 mW and 50%, respectively.

To investigate the time-domain characteristics of the dual-wavelength mode-locked output, we recorded oscilloscope pulse traces. As shown in Figure 3e, at a polarization direction of 60°, the pulse train period was 70 ns, indicating the fundamental mode-locking state of S1. In this case, the pulses of S2 were not observable in the oscilloscope, likely due to the weaker signal, which is also indicated in Figure 3b. However, in Figure 3f, when the polarization direction was set to 170°, two sets of pulse sequences were stable, each with a 70 ns pulse period.

Optical Switching. We studied the potential of anisotropic tellurene for use as an in-line optical switching device in optical fiber systems, which is a crucial element for signal processing in various applications such as optical communications and computing. Our experimental setup is shown in Figure 4a, where a 1550 nm light serves as the signal light and a 980 nm light acts as the control beam. These two lights are incident on the optical path through a wavelength division multiplexer (WDM). Within this path, two in-line tellurene nanosheets with a random lattice orientation are inserted. A 1550 nm filter along with a second WDM isolates the 980 nm control light, preventing it from interfering with the 1550 nm signal light. By adjusting a polarization controller positioned between the two twisted flakes, the transmission of the 1550 nm light is minimized, making the configuration of the two tellurene nanosheets and the polarization controller equivalent to those of two orthogonally twisted tellurenes. When the 980 nm light is incident on the first tellurene, the in-plane angle between the two nanosheets changes due to the anisotropic thermo-optical effect, causing significant modulation of the 1550 nm transmission light.

Figure 4b−e illustrates the modulation process of the 1550 nm light by the 980 nm control light. The control light is a square-wave with a period of 0.02 s and a 50% duty cycle, as depicted in Figure 4b. The corresponding modulated light is captured in Figure 4b, clearly demonstrating that the 1550 nm light is effectively modulated by the 980 nm control light in a stable on/off mode. Notably, the modulation process is extremely rapid. In Figure 4c, both the rise and decay times are close to the resolution limit of the optical power (4096 points per second sampling rate, corresponding to an interval of ∼244 μs). This indicates an ultrafast switching process that

https://doi.org/10.1021/acsnano.4c03973
ACS Nano XXXX, XXX, XXX−XXX

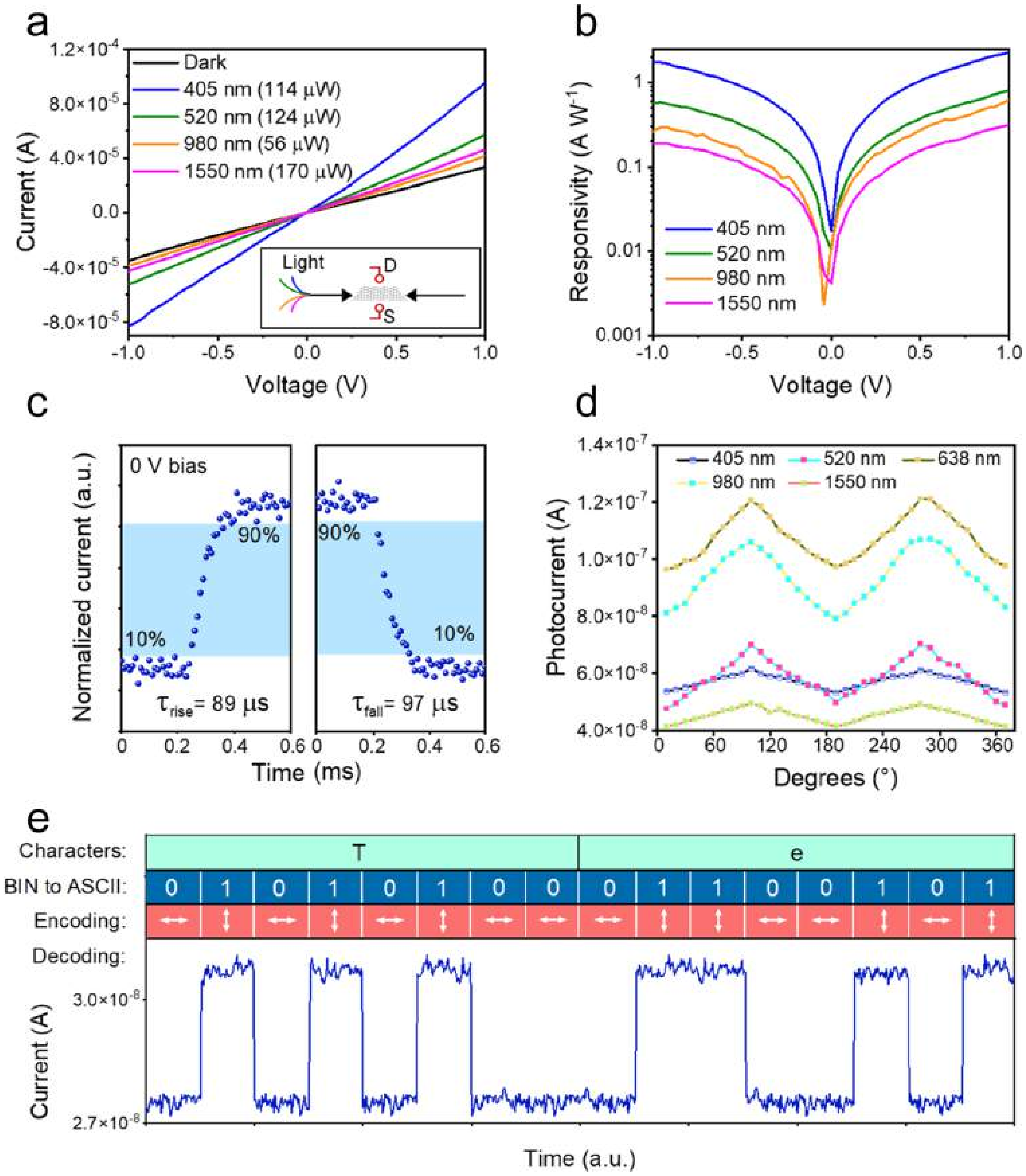

Figure 5. Photoelectric properties and bipolar polarization encoding communication application of a tellurene nanosheet-based photodetector. (a) Current−voltage curves of a tellurene nanosheet-based photodetector in the dark condition and under laser irradiation with different wavelengths. The insert provides a simple depiction of the test device diagram. (b) Responsivity−voltage curves of the tellurene nanosheet-based photodetector under different laser irradiation. (c) Rise and fall times of the tellurene nanosheet-based photodetector at 0 V bias. (d) Polarized photocurrent of the tellurene nanosheet-based photodetector under different incident wavelengths. (e) Bipolar polarization encoding communication application of the tellurene nanosheet-based photodetector, with the horizontal and vertical polarized laser irradiation encoded as "0" and "1", respectively.

outperforms similar devices based on other 2D materials and structures. For example, with similar configurations, the response times of optical switches based on WS_2 and graphene are ~7.3 and 9.1 ms, respectively. For biologically synthesized tellurium, a fast response time of 276.3−563.0 μs is reported, which is still slower than our report. The anisotropic thermo-optic effect in tellurene nanosheets enables effective modulation of 1550 nm light with exceptional speed and stability, outperforming similar devices based on other 2D materials.

The primary mechanism behind our tellurene-based optical switch is the anisotropic thermo-optic effect. This effect causes a change in the in-plane angle between the two tellurene nanosheets when 980 nm light is incident on the first nanosheet, leading to significant modulation of the 1550 nm transmission light. To further ascertain the origin of the light modulation capability in the twisted tellurene-based optical switch, we conducted measurements on the output power of the 1550 nm modulated light as a function of both the duty cycle and optical power of the 980 nm control pulses. When the power of the control light was fixed and different duty cycles were varied from 10 to 60%, the on/off ratio of the 1550 nm modulated light maintained a constant value, whereas the

https://doi.org/10.1021/acsnano.4c03973
ACS Nano XXXX, XXX, XXX−XXX

duty cycles of the 1550 nm modulated light exhibited a similar varying trend (refer to Figure 4d). Moreover, as depicted in Figure 4f,g, with the increase of the control light power from 200 to 250 mW, the switching ratio correspondingly increased from 1.21 to 1.34. Additionally, there was a linear increase in the on/off ratio with the augmentation of the input signal pulse power. Furthermore, the output power of the Te optical switch strongly correlated with the signal pulse power. As illustrated in Figure 4e, when the control light power was fixed at 200 mW and the duty cycle remained constant, the output power of the optical switch exhibited a linear relationship with varying signal light. These observations align with previous experimental measurements reported in other thermo-optical devices, indicating that the anisotropic thermo-optical effect is the primary mechanism behind our tellurene-based optical switch. Furthermore, Figure S5 demonstrates that the thickness of Te not only affects the transmittance of polarized light but also significantly impacts the switching ratio of optical switches. Specifically, 50 nm tellurene exhibits exceptional performance with a light transmittance three times greater than that of 90 nm tellurene. Correspondingly, its switching ratio is also 2.5 times higher than that of 90 nm tellurene. We then performed a measurement to assess the switching stability (Figure 4h), which showed the modulation of a 1550 nm pulse train by a control beam with a 50% duty cycle over 800 ms. The modulated pulses remained stable throughout the assessment, affirming the switching stability of our tellurene-based optical device.

In-Line Polarization Photodetector. The tellurene nanosheet-based in-line device demonstrates its capability as a polarized-sensitive photodetector. The systematic acquisition of source−drain current values under both dark and light illumination conditions is presented through the $I-V$ characteristics (Figure 5a). Notably, a pronounced photoresponse in current is evident across a wavelength ranging from 405 to 1550 nm. The device displayed a nearly linear correlation between the current and applied voltage, indicating favorable contact between tellurene nanosheets and gold electrodes and its operation state of a photoconductive mode. The corresponding responsivities under diverse incident wavelengths are delineated in Figure 5b, demonstrating significant responsivities of approximately ∼2 A W^{-1} at 405 nm and ∼0.2 A W^{-1} at 1550 nm under a 1.0 V bias condition.

Under bias-free conditions, the photodetector also exhibits a photoresponse across visible and near-infrared wavelengths (Figure S6a, enlarged view of the curves around zero bias in Figure 5a). The system's asymmetry between electrodes with the fiber core contributes to the generation of a self-driven photocurrent. Figure S6b shows the photoswitching characteristics under 0 V bias at 1550 nm Photoswitching characteristics under 0 V bias at 1550 nm are presented in Figure S6b, showcasing consistent and reliable photoswitching for both "on" and "off" currents under varying irradiation intensities. The device's responsivity and noise equivalent power (NEP) under diverse light power conditions are portrayed in Figure S6c when operating in the self-driven mode. Even under the self-driven mode operation, the fiber-compatible photodetector maintains a low NEP and a high responsivity (∼10^{-11} W $Hz^{-1/2}$ and 0.2 mA W^{-1} at 1550 nm, respectively).

The rise time (τ_{rise}) and fall time (τ_{fall}), essential parameters representing the response speed and work bandwidth, are depicted in Figure 5c. By recording a single circle of the ON/OFF state via an oscilloscope, the rise time and fall time under self-driven mode are demonstrated to be 89 and 97 μs, respectively, in which the response speed surpasses that of fiber-coupled photodetectors based on other 2D materials reported previously.[40−42] The repaid response may be attributed to the fast separation and transportation of photogenerated carriers within the tellurene material.

Given the pronounced anisotropy in the light absorption of tellurium arising from its inherent anisotropic nature, we conducted a systematic exploration of the polarized photocurrent in the tellurene nanosheet-based photodetector across various wavelengths, as illustrated in Figure 5d. A distinct polarized response was unequivocally observed within the wavelength range of 405−1550 nm. The degree of polarization achieved by the self-powered photodetector reached approximately ∼1.48 at 520 nm and ∼1.2 at 1550 nm, as shown in Figure S6d. We also performed a numerical simulation based on a two-probe device model and further provided evidence that the polarized photodetection originated from the lattice anisotropy of tellurene (Figure S7).

Leveraging the rapid and polarized response exhibited by a tellurene-based photodetector at 1550 nm, we performed a polarization encoding procedure for optical communication via an 8-bit code unit. The original signal was adeptly restored and conveyed through the deciphering unit by establishing a judicious threshold current. In this unipolar coding demonstration, we assigned signal values "0" and "1" to LP-0° and LP-90°, respectively. The information encoded in the current values was then interpreted as " tellurene" based on the American Standard Information Exchange Code (ASCII), as illustrated in Figure 5e. This underscores the potential of tellurene nanosheets for secure and efficient data transmission through the exploitation of polarized optical signals in encoded communication systems.

CONCLUSIONS

In conclusion, the fiber in-line optical device, based on a single-crystalline tellurene nanosheet, demonstrates versatile functionalities driven by the material's unique low-symmetry lattice structure and optical anisotropy. The device adeptly generates diverse optical outputs, including linearly polarized mode-locking pulses, dual-wavelength mode-locking pulses, efficient optical switching, and high-performance broadband polarization photodetection. Stable pulses with a duration of 770 fs and a DOP of 98% can be achieved by inserting the optical device into a 1.5 μm fiber laser. Adjusting the intracavity polarization state results in dual-wavelength mode-locking pulses, producing two separate pulse trains with a peak wavelength interval exceeding 10 nm. Additionally, all-optical switching operations are achieved through a twisted configuration of two tellurene nanosheets with a fast response time of less than 200 μs. For the photodetection function, highly sensitive and fast photodetection across a range from 520 to 1550 nm is achieved under zero-bias conditions, with potential implications in bipolar polarization encoding communication. Our results establish a promising prototype for integrating polarization as an additional physical dimension in fiber optical networks through the utilization of anisotropic 2D tellurene, encompassing diverse applications in light generation, modulation, and detection.

METHODS/EXPERIMENTS

Tellurene Nanosheets. To construct saturable absorber devices, the synthesis process of tellurene nanosheets was first carried out

https://doi.org/10.1021/acsnano.4c03973
ACS Nano XXXX, XXX, XXX−XXX

using a modified solution growth method. The length and width of tellurene nanosheets can be controlled by the reaction time and ratio of precursors. Specifically, the precursors Na_2TeO_3 (0.45 M) and poly(vinylpyrrolidone) (PVP, K30, 0.012 M) were dissolved in deionized water by magnetic stirring, a certain amount of ammonia–water (25–28%, wt/wt %) was added, and hydrazine hydrate (N_2H_4, 80%, wt/wt %) was used to adjust the pH (pH ~10) until a homogeneous solution formed. Then, the mixed transparent solution was poured into a Teflon-lined stainless-steel autoclave, and the sealed autoclave was kept at 180 °C for 24 h. Finally, after the autoclave was naturally cooled to room temperature, the resulting blue-black suspension was centrifuged at 7000 rpm for 5 min to obtain a silver-gray solid preproduct. Following three washes with deionized water to remove residual reactants, tellurene nanosheets with a clean surface were obtained.

Device Preparation. The tellurene nanosheet solution was uniformly dispersed on a Si substrate with monomolecular modification by the suspension coating method. The sample was then glued to the glass sheet using PVC, which is a key step in the subsequent material transfer. Poly(vinyl chloride) solution (PVC) was selected as the medium because of its suitable viscosity and transparency. Prior to transfer, the crystals were examined through transparent PVC substrates under an optical microscope to select samples of suitable size and high quality. The PVC substrate was very gently and slowly peeled off when the selected tellurene sheet was aligned with and in contact with the fiber ferris (or the fiber that is laterally polished). The selected 2D tellurene wafer will separate from the PVC and adhere to the core region of the fiber end-face due to van der Waals forces (see Figure S2). It should be noted that 2D tellurene flakes can remain intact after the dry transfer process. Thus, the saturated absorber device was prepared.

Passively Mode-Locked Fiber Lasers. The gain fiber of the ring cavity was 0.9 m EDF (Er80-9/125, Nufern), and the absorption coefficient at 976 nm was ~80 dB m^{-1}. The other fiber was a 12.84 m long single-mode fiber (SMF) with a group velocity dispersion (GVD) parameter of 18 (ps/nm)/km. The cavity was pumped by a 980 nm laser diode with a maximum power of 540 mW. A 980/1550 nm pump wavelength division multiplexer (WDM) was used to couple the pump light to the fiber cavity. To optimize the birefringent properties of optical fibers using an intracavity polarization controller, a nonpolarizing isolator in the chamber enforces the unidirectional operation of the chamber. The laser output was extracted from the 10% port of the 90:10 PM (Polarization Maintaining) coupler.

ASSOCIATED CONTENT

Supporting Information

The Supporting Information is available free of charge at https://pubs.acs.org/doi/10.1021/acsnano.4c03973.

> Material characterizations of tellurene, including AFM, Raman, and optical transmittance results; experimental setup for characterizing the polarization state of the as-fabricated mode-locked fiber lasers; effect of thickness of the Te nanosheet on the output of the Te optical switch; additional performance characteristics of a tellurene nanosheets-based photodetector; and numerical simulation results of the tellurene-based photodetector (PDF)

AUTHOR INFORMATION

Corresponding Authors

Haoran Mu – *Songshan Lake Materials Laboratory, Dongguan 523808, China*; Email: muhaoran@sslab.org.cn

Sheng Lan – *Guangdong Provincial Key Laboratory of Nanophotonic Functional Materials and Devices, School of Information and Optoelectronic Science and Engineering, South China Normal University, Guangzhou 510006, China*; orcid.org/0000-0002-7277-0042; Email: slan@scnu.edu.cn

Shenghuang Lin – *Songshan Lake Materials Laboratory, Dongguan 523808, China*; orcid.org/0000-0001-9552-4680; Email: linshenghuang@sslab.org.cn

Authors

Jing Yu – *Songshan Lake Materials Laboratory, Dongguan 523808, China; Guangdong Provincial Key Laboratory of Nanophotonic Functional Materials and Devices, School of Information and Optoelectronic Science and Engineering, South China Normal University, Guangzhou 510006, China*

Pu Wang – *Songshan Lake Materials Laboratory, Dongguan 523808, China*

Haozhe Li – *Songshan Lake Materials Laboratory, Dongguan 523808, China*

Zixin Yang – *College of Advanced Interdisciplinary Studies, National University of Defense Technology, Changsha 410073, China*

Jing Ren – *Songshan Lake Materials Laboratory, Dongguan 523808, China*

Yang Li – *Songshan Lake Materials Laboratory, Dongguan 523808, China*

Luyao Mei – *Songshan Lake Materials Laboratory, Dongguan 523808, China*

Jingni Zhang – *Songshan Lake Materials Laboratory, Dongguan 523808, China*

Wenzhi Yu – *Songshan Lake Materials Laboratory, Dongguan 523808, China*

Nan Cui – *Songshan Lake Materials Laboratory, Dongguan 523808, China*

Jian Yuan – *State Key Laboratory of Applied Optics, Changchun Institute of Optics, Fine Mechanics and Physics, Chinese Academy of Sciences, Changchun 130033, China*

Jian Wu – *College of Advanced Interdisciplinary Studies, National University of Defense Technology, Changsha 410073, China*; orcid.org/0000-0003-3747-7358

Guangyu Zhang – *Songshan Lake Materials Laboratory, Dongguan 523808, China*

Complete contact information is available at: https://pubs.acs.org/10.1021/acsnano.4c03973

Author Contributions

⊥J.Y., H.M., and P.W. contributed equally to this work. H.M. and S.L. conceived the idea and supervised the project. H.M. designed the experiments. P.W. prepared the tellurene nanosheet and carried out material characterizations. J.Y. and H.M. carried out device fabrication and optical device performance characterizations. H.L., J.R., J.Z., and N.C. helped transfer of the tellurene materials. H.M. and W.Y. carried out the characterizations of the photodetector. J.W. performed the simulation. H.M., S.L., and G.Z. wrote the manuscript with input from all authors.

Notes

The authors declare no competing financial interest.

ACKNOWLEDGMENTS

We acknowledge the support from the National Natural Science Foundation of China (No. 12204336), the Guangdong Basic and Applied Basic Research Foundation (Nos. 2024A1515010350 and 2021B1515120034), the National Key R&D Program of China (No. 2021YFA1202902), Songshan Lake Materials Laboratory (No. Y0D1051F211), the State Key Laboratory of Applied Optics (SKLAO2022001A13), and the Natural Science Foundation of Anhui Higher Education Institutions of China (2023AH050335, 2022AH050379, and 2023AH050349).

REFERENCES

(1) Biswas, S.; Grajower, M. Y.; Watanabe, K.; Taniguchi, T.; Atwater, H. A. Broadband electro-optic polarization conversion with atomically thin black phosphorus. *Science* **2021**, *374* (6566), 448–453.

(2) Flöry, N.; Ma, P.; Salamin, Y.; Emboras, A.; Taniguchi, T.; Watanabe, K.; Leuthold, J.; Novotny, L. Waveguide-integrated van der Waals heterostructure photodetector at telecom wavelengths with high speed and high responsivity. *Nat. Nanotechnol.* **2020**, *15* (2), 118–124.

(3) Datta, I.; Chae, S. H.; Bhatt, G. R.; Tadayon, M. A.; Li, B.; Yu, Y.; Park, C.; Park, J.; Cao, L.; Basov, D.; et al. Low-loss composite photonic platform based on 2D semiconductor monolayers. *Nat. Photonics* **2020**, *14* (4), 256–262.

(4) Chen, J.-h.; Xiong, Y.-f.; Xu, F.; Lu, Y.-q. Silica optical fiber integrated with two-dimensional materials: towards opto-electro-mechanical technology. *Light: Sci. Appl.* **2021**, *10* (1), 78.

(5) Mu, H.; Liu, Y.; Bongu, S. R.; Bao, X.; Li, L.; Xiao, S.; Zhuang, J.; Liu, C.; Huang, Y.; Dong, Y.; et al. Germanium nanosheets with dirac characteristics as a saturable absorber for ultrafast pulse generation. *Adv. Mater.* **2021**, *33* (32), No. 2101042.

(6) Zuo, Y.; Yu, W.; Liu, C.; Cheng, X.; Qiao, R.; Liang, J.; Zhou, X.; Wang, J.; Wu, M.; Zhao, Y.; et al. Optical fibres with embedded two-dimensional materials for ultrahigh nonlinearity. *Nat. Nanotechnol.* **2020**, *15* (12), 987–991.

(7) An, N.; Tan, T.; Peng, Z.; Qin, C.; Yuan, Z.; Bi, L.; Liao, C.; Wang, Y.; Rao, Y.; Soavi, G.; Yao, B. Electrically tunable four-wave-mixing in graphene heterogeneous fiber for individual gas molecule detection. *Nano Lett.* **2020**, *20* (9), 6473–6480.

(8) Mu, H.; Liu, Z.; Bao, X.; Wan, Z.; Liu, G.; Li, X.; Shao, H.; Xing, G.; Shabbir, B.; Li, L.; et al. Highly stable and repeatable femtosecond soliton pulse generation from saturable absorbers based on two-dimensional $Cu_{3-x}P$ nanocrystals. *Front. Optoelectron.* **2020**, *13*, 139–148.

(9) Shah, M. K.; Ye, S.-W.; Zou, X.-H.; Yuan, F.; Jha, A.; Zhang, Y. L.; Lu, R.-G.; Liu, Y. Graphene-assisted electroabsorption optical modulator using D-microfiber. *IEEE J. Sel. Top. Quantum Electron.* **2017**, *23* (1), 89–93.

(10) Li, W.; Chen, B.; Meng, C.; Fang, W.; Xiao, Y.; Li, X.; Hu, Z.; Xu, Y.; Tong, L.; Wang, H.; et al. Ultrafast all-optical graphene modulator. *Nano Lett.* **2014**, *14* (2), 955–959.

(11) Jin, Z.; Ye, F.; Zhang, X.; Jia, S.; Dong, L.; Lei, S.; Vajtai, R.; Robinson, J. T.; Lou, J.; Ajayan, P. M. Near-field coupled integrable two-dimensional InSe photosensor on optical fiber. *ACS Nano* **2018**, *12* (12), 12571–12577.

(12) Wang, X.; Lan, S. Optical properties of black phosphorus. *Adv. Opt. Photonics* **2016**, *8* (4), 618–655.

(13) Al-Hattab, M.; Moudou, L.; Chrafih, Y.; Khenfouch, M.; Bajjou, O.; Rahmani, K. The anisotropic optical properties of different polytypes (ε, β, δ, γ) of GaSe lamellar materials. *Eur. Phys. J. Appl. Phys.* **2020**, *91* (3), 30102.

(14) Cai, C.; Ling, S.; Hou, P. In-plane anisotropic photoelectric property of α-In_2Se_3 based phototransistor. *Appl. Phys. Lett.* **2023**, *122* (19), No. 192101.

(15) Lin, Y.-C.; Komsa, H.-P.; Yeh, C.-H.; Bjorkman, T.; Liang, Z.-Y.; Ho, C.-H.; Huang, Y.-S.; Chiu, P.-W.; Krasheninnikov, A. V.; Suenaga, K. Single-layer ReS_2: two-dimensional semiconductor with tunable in-plane anisotropy. *ACS Nano* **2015**, *9* (11), 11249–11257.

(16) Agrell, E.; Karlsson, M.; Chraplyvy, A.; Richardson, D. J.; Krummrich, P. M.; Winzer, P.; Roberts, K.; Fischer, J. K.; Savory, S. J.; Eggleton, B. J.; et al. Roadmap of optical communications. *J. Opt.* **2016**, *18* (6), No. 063002.

(17) Winzer, P. J. Spatial multiplexing in fiber optics: The 10x scaling of metro/core capacities. *Bell Syst. Technol. J.* **2014**, *19*, 22–30.

(18) Beygi, L.; Agrell, E.; Karlsson, M.; Johannisson, P. Signal statistics in fiber-optical channels with polarization multiplexing and self-phase modulation. *J. Lightwave Technol.* **2011**, *29* (16), 2379–2386.

(19) Chen, Y.; Jiang, G.; Chen, S.; Guo, Z.; Yu, X.; Zhao, C.; Zhang, H.; Bao, Q.; Wen, S.; Tang, D.; Fan, D. Mechanically exfoliated black phosphorus as a new saturable absorber for both Q-switching and mode-locking laser operation. *Opt. Express* **2015**, *23* (10), 12823–12833.

(20) Qin, Z.; Xie, G.; Zhao, C.; Wen, S.; Yuan, P.; Qian, L. Mid-infrared mode-locked pulse generation with multilayer black phosphorus as saturable absorber. *Opt. Lett.* **2016**, *41* (1), 56–59.

(21) Ma, M.; Zhang, J.; Zhang, Y.; Wang, X.; Wang, J.; Yu, P.; Liu, Z.; Wei, Z. Ternary chalcogenide Ta_2NiS_5 nanosheets for broadband pulse generation in ultrafast fiber lasers. *Nanophotonics* **2020**, *9* (8), 2341–2349.

(22) Dai, Y.; Yu, Q.; Yang, X.; Guo, K.; Zhang, Y.; Zhang, Y.; Zhang, J.; Li, J.; Chen, J.; Deng, H.; et al. Controllable synthesis of narrow-gap van der waals semiconductor Nb_2GeTe_4 with asymmetric architecture for ultrafast photonics. *ACS Nano* **2022**, *16* (3), 4239–4250.

(23) Autere, A.; Jussila, H.; Dai, Y.; Wang, Y.; Lipsanen, H.; Sun, Z. Nonlinear optics with 2D layered materials. *Adv. Mater.* **2018**, *30* (24), No. 1705963.

(24) Liu, H.; Li, Z.; Yu, Y.; Lin, J.; Liu, S.; Pang, F.; Wang, T. Nonlinear optical properties of anisotropic two-dimensional layered materials for ultrafast photonics. *Nanophotonics* **2020**, *9* (7), 1651–1673.

(25) Li, D.; Jussila, H.; Karvonen, L.; Ye, G.; Lipsanen, H.; Chen, X.; Sun, Z. Polarization and thickness dependent absorption properties of black phosphorus: new saturable absorber for ultrafast pulse generation. *Sci. Rep.* **2015**, *5* (1), No. 15899.

(26) Wang, Y.; Qiu, G.; Wang, R.; Huang, S.; Wang, Q.; Liu, Y.; Du, Y.; Goddard III, W. A.; Kim, M. J.; Xu, X.; et al. Field-effect transistors made from solution-grown two-dimensional tellurene. *Nat. Electron.* **2018**, *1* (4), 228–236.

(27) Wu, W.; Qiu, G.; Wang, Y.; Wang, R.; Ye, P. Tellurene: its physical properties, scalable nanomanufacturing, and device applications. *Chem. Soc. Rev.* **2018**, *47* (19), 7203–7212.

(28) Yan, Z.; Yang, H.; Yang, Z.; Ji, C.; Zhang, G.; Tu, Y.; Du, G.; Cai, S.; Lin, S. Emerging Two-Dimensional Tellurene and Tellurides for Broadband Photodetectors. *Small* **2022**, *18* (20), No. 2200016.

(29) Deckoff-Jones, S.; Wang, Y.; Lin, H.; Wu, W.; Hu, J. Tellurene: a multifunctional material for midinfrared optoelectronics. *ACS Photonics* **2019**, *6* (7), 1632–1638.

(30) Lu, J.; He, Y.; Ma, C.; Ye, Q.; Yi, H.; Zheng, Z.; Yao, J.; Yang, G. Ultrabroadband imaging based on wafer-scale tellurene. *Adv. Mater.* **2023**, *35* (20), No. 2211562.

(31) Tong, L.; Huang, X.; Wang, P.; Ye, L.; Peng, M.; An, L.; Sun, Q.; Zhang, Y.; Yang, G.; Li, Z.; et al. Stable mid-infrared polarization imaging based on quasi-2D tellurium at room temperature. *Nat. Commun.* **2020**, *11* (1), No. 2308.

(32) Wang, K.; Zhang, X.; Kislyakov, I. M.; Dong, N.; Zhang, S.; Wang, G.; Fan, J.; Zou, X.; Du, J.; Leng, Y.; et al. Bacterially synthesized tellurium nanostructures for broadband ultrafast nonlinear optical applications. *Nat. Commun.* **2019**, *10* (1), No. 3985.

(33) He, P.; Hu, X.; Hu, Z.; Chen, J.; Xie, Z.; Huang, J.; Tao, L.; Lu, H.; Hao, M. Preparation of tellurium nanowires and its application in ultrafast photonics. *J. Lumin.* **2022**, *252*, No. 119335.

(34) Xu, N.; Ma, P.; Fu, S.; Shang, X.; Jiang, S.; Wang, S.; Li, D.; Zhang, H. Tellurene-based saturable absorber to demonstrate large-energy dissipative soliton and noise-like pulse generations. *Nanophotonics* **2020**, *9* (9), 2783–2795.

(35) Guo, J.; Zhao, J.; Huang, D.; Wang, Y.; Zhang, F.; Ge, Y.; Song, Y.; Xing, C.; Fan, D.; Zhang, H. Two-dimensional tellurium–polymer membrane for ultrafast photonics. *Nanoscale* **2019**, *11* (13), 6235–6242.

(36) Hu, H.; Zeng, Y.; Gao, S.; Wang, R.; Zhao, J.; You, K.; Song, Y.; Xiao, Q.; Cao, R.; Li, J.; Lin, Z.; Guo, J.; Shu, Y.; Guo, Z.; Fan, D. Fast solution method to prepare hexagonal tellurium nanosheets for optoelectronic and ultrafast photonic applications. *J. Mater. Chem. C* **2021**, *9* (2), 508−516.
(37) Zhang, W.; Wang, G.; Xing, F.; Man, Z.; Zhang, F.; Han, K.; Zhang, H.; Fu, S. Passively Q-switched and mode-locked erbium-doped fiber lasers based on tellurene nanosheets as saturable absorber. *Opt. Express* **2020**, *28* (10), 14729−14739.
(38) Wang, K.; Zhang, X.; Kislyakov, I. M.; Dong, N.; Zhang, S.; Wang, G.; Fan, J.; Zou, X.; Du, J.; Leng, Y.; Zhao, Q.; Wu, K.; Chen, J.; Baesman, S. M.; Liao, K.-S.; Maharjan, S.; Zhang, H.; Zhang, L.; Curran, S. A.; Oremland, R. S.; Blau, W. J.; Wang, J. Bacterially synthesized tellurium nanostructures for broadband ultrafast non-linear optical applications. *Nat. Commun.* **2019**, *10* (1), No. 3985.
(39) Hassan, H.; Munshid, M. A.; Al-Janabi, A. Tellurium-nanorod-based saturable absorber for an ultrafast passive mode-locked erbium-doped fiber laser. *Appl. Opt.* **2020**, *59* (4), 1230−1236.
(40) Chen, J.-h.; Liang, Z.-h.; Yuan, L.-r.; Li, C.; Chen, M.-r.; Xia, Y.-d.; Zhang, X.-j.; Xu, F.; Lu, Y.-q. Towards an all-in fiber photodetector by directly bonding few-layer molybdenum disulfide to a fiber facet. *Nanoscale* **2017**, *9* (10), 3424−3428.
(41) Xiong, Y. F.; Chen, J. H.; Lu, Y. Q.; Xu, F. Broadband optical-fiber-compatible photodetector based on a graphene-MoS_2-WS_2 heterostructure with a synergetic photogenerating mechanism. *Adv. Electron. Mater.* **2019**, *5* (1), No. 1800562.
(42) Yang, H.; Xiao, Y.; Zhang, K.; Chen, Z.; Pan, J.; Zhuo, L.; Zhong, Y.; Zheng, H.; Zhu, W.; Yu, J.; Chen, Z. Self-powered and high-performance all-fiber integrated photodetector based on graphene/palladium diselenide heterostructures. *Opt. Express* **2021**, *29* (10), 15631−15640.

https://doi.org/10.1021/acsnano.4c03973
ACS Nano XXXX, XXX, XXX−XXX